ISSN 1023-1935, Russian Journal of Electrochemistry, 2012, Vol. 48, No. 7, pp. 712–726. © Pleiades Publishing, Ltd., 2012.
Published in Russian in Elektrokhimiya, 2012, Vol. 48, No. 7, pp. 786–800.

Numerical Investigation of Liquid Water Transport and Distribution in Porous Gas Diffusion Layer of a Proton Exchange Membrane Fuel Cell Using Lattice Boltzmann Method[1]

Li Chen, Hui-Bao Luan, Ya-Ling He, and Wen-Quan Tao[z]

Key Laboratory of Thermal Fluid Science and Engineering of MOE School of Energy and Power Engineering, Xi'an Jiaotong University, Xi'an, Shaanxi 710049, China

Received May 30, 2011

Abstract—Lattice Boltzmann method (LBM) is used to investigate liquid water transport and distribution in a porous gas diffusion layer (GDL). The GDL with microscopic porous structures is obtained from three-dimensional reconstruction using the stochastic method, and its macroscopic transport properties including permeability and effective diffusivity are numerically predicted which agree well with the existing experimental results. Simulation results show that liquid water transport mechanism in the GDL is capillary fingering and liquid water pathway is interconnected, which confirms the previous experimental results in literature. Further, effects of GC wettability are explored and it is found out that a hydrophilic GC leads to less liquid water accumulated in the GDL compared with a hydrophobic GC. In addition, effects of GDL wettability on liquid water distribution are explored. Simulation results show that PTFE content itself cannot determine liquid water distribution inside the GDL and detailed distributions of hydrophobic and hydrophilic regions within the GDL also play an import role. Moreover, a hydrophilic GDL is more beneficial for reactant transport than a hydrophobic GDL if liquid water presents as separated droplets or films in the GDL.

Keywords: Proton exchange membrane fuel cell; lattice Boltzmann method; gas diffusion layer; liquid water; wettability

DOI: 10.1134/S1023193512070026

1. INTRODUCTION

The proton exchange membrane fuel cell (PEMFC) is a promising candidate of the power source for a range of applications because of its notable advantages such as high power density, high efficiency, low operation temperature, low noise and no pollutions. However, PEMFC requires further improvements to achieve wide commercial use, particularly in regard of the cell performance. To improve performance of PEMFC, proper thermal and water managements are urgently demanded.

Successful water management in the PEMFC, particularly in the cathode side, is crucial to the cell performance, as poor water management results in either dehydration of membrane or flooding issues. On the one hand, membrane dehydration increases the proton conductive resistance and thus reduces the cell performance owing to great ohmic loss across the membrane. On the other hand, however, flooding problems occur if excessive liquid water accumulates in the components of a PEMFC including gas channel (GC), gas diffusion layer (GDL), and catalyst layer (CL). Flooding can seriously debilitate cell performance which concretely presents as three sub-category flooding issues. On the microscopic scale, liquid water covers the CL surface, creating hindered oxygen transport and reduced reactive surface. On the mesoscopic scale, liquid water clogs pores of GDL, decreasing the effective transport of gaseous reactant to the reactive site. On the macroscopic scale, liquid water blocks the GC, resulting in mal-distributton of oxygen and an increase in parasitic pumping power to overcome the increased pressure drop. Therefore, many researches have highlighted and emphasized the requirement of proper water management, and extensive studies have endeavored to investigate liquid water transport processes in the components of a PEMFC. Reviews of these studies have been conducted in [1–3].

The transport of liquid water within the GDL is one of the most important water management issues in PEMFC. Commonly used GDL materials for a PEMFC are carbon fiber based carbon paper (shown in Fig. 1) and carbon cloth. In order to facilitate the removal of liquid water, GDL is usually treated with a non-wetting polymer such as polytetrafluoroethylene (PTFE) to make them hydrophobic. The transport of liquid water through a GDL is a drainage process in which the non-wetting liquid water displaces the wet-

[1] The article is published in the original.

[z] Corresponding author: wqtao@mail.xjtu.edu.cn (Wen-Quan Tao).

ting air. The displacement is dominated by capillary forces due to the low water flow rate and narrow void space within the GDL. Under typical PEMFC operating conditions, the capillary number Ca (ratio of viscous force to surface tension force, $Ca = \mu u/\sigma$, with μ water dynamic viscosity, u liquid water velocity, σ surface tension between water and air) is of the order 10^{-6}–10^{-8} and the viscosity ratio M ($M = \mu_{water}/\mu_{air}$) is about 17.5, leading to capillary fingering in the GDL according to the phase diagram for drainage flow proposed by Lenormand [4]. There have been some experimental researches regarding liquid water transport dynamics within the GDL [5–9]. Nam and Kaviany [5] suggested a branching-type geometry of liquid water distribution, in which water vapor condenses on GDL surfaces and forms micro-droplets which then agglomerate to large macro-droplets. These macro-droplets then connect to each other and form continuous liquid water flow which moves by occupying the largest pores on its advancing path. A similar liquid water distribution inside the GDL was also proposed by Pasaogullari and Wang [10]. On the other hand, Lister et al. [6] proposed another mechanism called as fingering and channeling. In this mechanism, liquid water generated by electrochemical reactions builds up pressure and preferentially breaks through the pores with the largest diameter. A preferential pathway is formed after the liquid water permeates through the GDL along the through-plane direction and numerous "dead ends" exist in the GDL. Moreover, liquid water distribution within the GDL is dynamic interconnected and the preferential pathway of liquid water evolves with time [7, 8]. Recently, in situ experiments using synchrotron X-ray radiography confirmed the coexistence of the above two liquid water transport mechanisms [11]. In addition, phase-change-induced flow in the GDL also has been reported recently [12–14]. Actually, liquid water transport in the GDL is significantly complicated due to the anisotropic microstructures of GDL and [illegible] bility within the GDL along with vario[illegible] conditions [15, 16].

Recently, there have been some researches trying to investigate fluid flow and mass transport in the GDL based on pore-scale simulation in which the microstructures of GDL are considered using lattice Boltzmann method (LBM). LBM has been a powerful numerical scheme to investigate flow and mass transport in GDL owing to its unique ability of simulating based on the real complex pore structures [17]. Generally, GDL presents inhomogeneous properties such as different in-plane and through-plane permeabilities due to its antistrophic structures. Thus, LBM has been used to numerically predict the in-plane and through-plane permeabilities of the GDL [18, 19]. In addition, liquid water transport and distribution in the GDL are investigated using LBM [20–24]. Park and Li [20] explored behaviors of a droplet passing through porous structures of a carbon paper GDL based on 2D simulation. Further, some researches investigated liquid water transport processes in 3D reconstructed GDL [21–24]. Moreover, liquid water transport and distribution in GDL with mixed wettability were also explored using LBM [22–24]. These researches indeed presented a detailed insight into the pore-scale information of flow and mass transport within the GDL, although simulations using LBM always require huge computational resources.

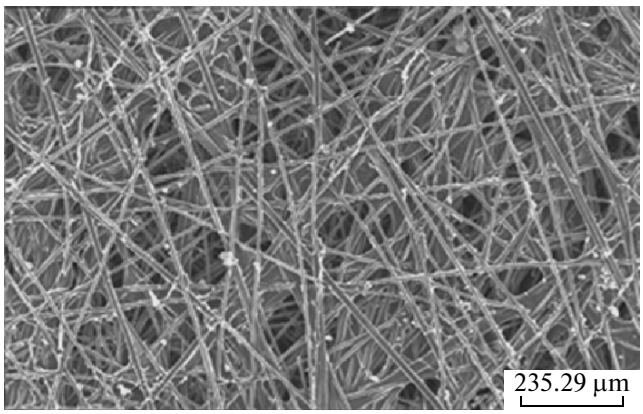

Fig. 1. A scanning electron microscope (SEM) image of a carbon paper GDL.

In this study, LBM is used to investigate liquid water dynamic behaviors in a porous carbon paper GDL. Effects of land wettability and GDL wettability on liquid water distributions are explored. The following part of this paper is organized as follows: LBM models used in this study are briefly introduced in Section 2. Computational domain is also introduced in Section 2. Then in Section 3 liquid water transport in GDL and gas channel without land, in GDL and gas channel with a land, and in GDL with different wettability are studied. Finally, ~~a conclusion is obtained~~ in [illegible]

Corrected as: some conclusions are drawn

2. PHYSICAL AND MATHEMATICAL MODEL

2.1. Brief Introduction to LBM

During the last two decades, LBM has been developed as an alternative and powerful numerical scheme for a variety of fluid transport phenomena [17]. Unlike conventional CFD methods which solve discrete forms of the mass, momentum and energy conservation equations based on macroscopic quantities such as velocity and density, LBM simulates fluid particles on a mesoscopic level based on Boltzmann equation using a small number of velocities adapted to a regular grid in space. For completeness, only a brief introduction of LB models used in this study is given in the following paragraphs.

2.1.1. Fluid flow LB model. The flow LB model employed in this study is based on the simple and popular Bhatnagar–Gross–Krook (BGK) method [25].

DnQb lattice is adopted where n denotes the dimension and b represents the number of discrete velocities. The evolution equation for particle distribution function $f_i(x, t)$ is

$$f_i(x + \mathbf{e}_i\Delta t, t + \Delta t) - f_i(x, t) = -\frac{1}{\tau}[f_i(x, t) - f_i^{eq}(x, t)], \quad (1)$$

where Δt is the time increment and τ is the collision time related to the kinematical viscosity, $\mathbf{e}_i$ is the discrete velocities and is defined as (for D2Q9 model used in this study)

$$\mathbf{e}_i = \begin{cases} 0 & i = 0 \\ \cos\left[\frac{(i-1)\pi}{2}\right], \sin\left[\frac{(i-1)\pi}{2}\right] & i = 1, 2, 3, 4 \\ \sqrt{2}\left(\cos\left[\frac{(i-5)\pi}{2} + \frac{\pi}{4}\right], \sin\left[\frac{(i-5)\pi}{2} + \frac{\pi}{4}\right]\right) & \\ i = 5, 6, 7, 8 & \end{cases} \quad (2)$$

The equilibrium distribution function $f_i^{eq}(x, t)$ is given as

$$f_i^{eq} = w_i\rho\left[1 + \frac{\mathbf{e}_i \cdot \mathbf{u}}{(c_s)^2} + \frac{(\mathbf{e}_i \cdot \mathbf{u})^2}{2(c_s)^4} - \frac{\mathbf{u} \cdot \mathbf{u}}{2(c_s)^2}\right] \quad (3)$$

for D2Q9 model, weight factor w_i are $w_i = 4/9$, $i = 0$; $w_i = 1/9$, $i = 1, 2, 3, 4$; $w_i = 1/36$, $i = 5, 6, 7, 8$. c_s is the sound speed ($c_s = c/\sqrt{3}$, where c equals $\Delta x/\Delta t$). The fluid number density ρ and velocity u are obtained from the first and second moments of the particle distribution functions.

$$\rho = \sum_i f_i, \quad (4)$$

$$\rho\mathbf{u} = \sum_i f_i\mathbf{e}_i. \quad (5)$$

The kinematics viscosity in lattice unit is related to the collision time by

$$\nu = c_s^2(\tau_\nu - 0.5)\Delta t. \quad (6)$$

2.1.2. Mass transport LB model. For mass transport with reaction, the evolution equation of the distribution function is [26]

$$f_i(x + \mathbf{e}_i\Delta t, t + \Delta t) - f_i(x, t) = -\frac{1}{\tau}(f_i(x, t) - f_i^{eq}(x, t)) + S, \quad (7)$$

where S is the source term related to the reaction ~~and will be discussed in Section 4.3~~. The equilibrium distribution function $f_i^{eq}(x, t)$ is commonly chosen as [27]

$$f_{i,k}^{eq} = X_k[J_i + K_i\mathbf{e}_i \cdot \mathbf{u}], \quad (8)$$

where K_i is constant and equals 1/2 for two dimension simulation. Subscript k denotes the kth component and X_k is the mole fraction of kth component (the ratio between the concentration of k component and the total concentration). J is the rest fraction and is obtained from $\sum f_i = \sum f_i^{eq}$.

For mass transport simulation, the D2Q9 square lattice for 2D simulation can be reduced to D2Q5 square lattice without loss of accuracy [27]. Therefore, the discrete velocities are

$$\mathbf{e}_i = \begin{cases} 0 & i = 0 \\ \cos\left[\frac{(i-1)\pi}{2}\right], \sin\left[\frac{(i-1)\pi}{2}\right] & i = 1, 2, 3, 4, \end{cases} \quad (9)$$

and J_i in Eq. (8) is given by [27]

$$J_i = \begin{cases} J_0, & i = 0 \\ (1 - J_0)/4, & i = 1, 2, 3, 4, \end{cases} \quad (10)$$

where the rest fraction J_0 can be selected from 0 to 1. Species mole fraction X_k is obtained by

$$X_k = \sum_i f_{i,k}. \quad (11)$$

The diffusivity in lattice unit is related to the collision time by

$$D = C_Q(1 - J_0)(\tau_D - 0.5)\frac{\Delta x^2}{\Delta t}, \quad (12)$$

where C_Q is a lattice dependent coefficient and equals 1/2 for 2D simulation [27].

2.1.3. Multiphase LB model. In this study, multicomponent multiphase model with inter-particle forces proposed by Shan and Chen (SC model) [28, 29] is employed to investigate the two-phase flow in GDL. The inter-particle forces are included in the kinetics through a set of potentials. In SC model it is simple to involve these interactions by replacing $\mathbf{u}$ in Eq. (3) with

$$\mathbf{u}_k = \mathbf{u}' + \frac{\tau_k\mathbf{F}_k}{\rho_k}, \quad (13)$$

where k denotes the kth fluid component, $\mathbf{u}'$ is a common velocity for all of the phases (liquid water and air in this paper) defined as

$$\mathbf{u}' = \frac{\sum_k \rho_k\mathbf{u}_k/\tau_k}{\sum_k \rho_k/\tau_k}. \quad (14)$$

In Eq. (13), $\mathbf{F}_k$ is the total force acting on the kth phase which may include fluid-fluid surface tension force, fluid-solid adhesion and body forces. The total fluid-

Delete

fluid surface tension force acting on the particles of the kth component at lattice site x is defined as [30]

$$\mathbf{F}_{e,k} = -\psi_k(\rho_k(x)) \times \sum_{x'}\sum_{\bar{k}}^{s} G_{k\bar{k}}(x,x')\psi_{\bar{k}}(\rho_{\bar{k}}(x'))(x'-x). \quad (15)$$

The effective density $\psi_k(\rho_k)$ is defined as $\psi_k(\rho_k) = \rho_0[1-\exp(-\rho_k)\rho_0)]$. If only the surface tension forces between the nearest and next-nearest neighboring points are considered, G can be described as

$$G_{k\bar{k}}(x,x') = \begin{cases} 4g & |x-x'| = 1 \\ g & |x-x'| = \sqrt{2} \\ 0 & |x-x'| = 0, \end{cases} \quad (16)$$

where g controls the strength between fluids. The fluid-solid interaction force $\mathbf{F}_{a,k}$ is introduced to describe the interaction between kth fluid and solid walls [30]

$$\mathbf{F}_{a,k} = -\psi_k(\rho_k(x))\sum_{x'} W(x,x')s(x')(x'-x), \quad (17)$$

$$W(x,x') = \begin{cases} 4w & |x-x'| = 1 \\ w & |x-x'| = \sqrt{2} \\ 0 & |x-x'| = 0, \end{cases} \quad (18)$$

where s is an indicator function and equals 0 and 1 for pore and solid, respectively. The coefficient w, which controls the strength between fluid and wall, is positive for non-wetting fluid and negative for wetting fluid. Different wettability can be obtained by adjusting w.

After involving inter-particle forces in Eq. (13), the relationship between pressure and density becomes [29]

$$p = \rho c_s^2 + \frac{3}{2}\sum g_{k\bar{k}}\psi_k\psi_{\bar{k}}. \quad (19)$$

This can be considered as the equation of state (EOS) of a non-ideal fluid, which makes the separation of liquid phase and gas phase possible.

2.2. Computational Domain

In this study, a carbon paper GDL with complex porous structure obtained from 3D structure reconstruction process is used instead of a homogenous GDL. Figure 1 shows a SEM image of a carbon paper GDL. It can be observed that the thin long carbon fibers mainly align in the in-plane direction and few can be observed in the through-plane direction, producing laminated structure of the carbon paper GDL. Based on the observation of Fig. 1, following assumptions are made in the 3D ~~reconstructed~~ process for simplification: the carbon fibers are straight with fixed diameter, no fiber is orientated for the through-plane direction and intersecting carbon fibers are randomly distributed in the in-plane direction. Then, the reconstruction procedure is implemented by piling up several carbon fiber layers. Each of the carbon fiber layers can be generated by locating fibers with random positions and angles until the prescribed porosity in this layer is satisfied. Figure 2a shows a 3D GDL generated from the reconstruction with fiber diameter of 7 μm, porosity of 0.7 and total layer number of 24, where x or z is the in-plane direction and y is the through-plane direction.

Corrected as: reconstruction

In this study, 2D simulation is performed and the 2D structure of the GDL (as shown in Fig. 2b) can be obtained from a through-plane cross-section slice of the 3D reconstructed GDL. Obviously, 3D simulation of liquid water transport in the porous GDL is more desirable, but it requires extremely huge computational resources which is not easily available for the authors. Thus, only a 2D cross-section slice of the reconstructed 3D porous structure of the GDL is adopted. Although the slice loses some of the characteristic of the 3D porous structure (for example, the connectivity of the solid phase), simulation results in the following section show that physical properties such as in-plane and through-plane permeability of the slice agree well with the existing experimental results, validating the feasibility of simulating based on the 2D slice.

The 2D slice has a size of 790 × 168 μm and is meshed into 790 × 168 lattices. In order to avoid the effects of carbon fiber structure on fluid flow and mass transport, five additional lattice grids are added to the boundaries of the computational domain, leading to the final lattice grid 800 × 178, as shown in Fig. 2b. When investigating the effects of GC wettability on liquid water transport with the GDL, a GC with height as 500 μm is placed on the top of the GDL, thus the computational domain with GDL and GC has a size of 800 × 700 μm and the corresponding lattices are 800 × 700, as shown in Fig. 2c.

3. RESULTS AND DISCUSSION

In the LBM model, the simulation variables are in the lattice units instead of physical units. To connect the lattice space to physical space, length scale l_0, time scale t_0 and density scale ρ_0 are chosen in this study. Accordingly, the physical variables such as velocity u_p, pressure p_p, permeability k_p, viscosity ν_p and diffusivity D_p can be calculated from the quantities in lattice system (subscripted by L) as follows

$$u_p = u_L\frac{l_0}{t_0}, \quad p_p = p_L\rho_0\left(\frac{l_0}{t_0}\right)^2, \quad k_p = k_L l_0^2, \quad \nu_p = \nu_L\frac{l_0^2}{t_0}. \quad (20)$$

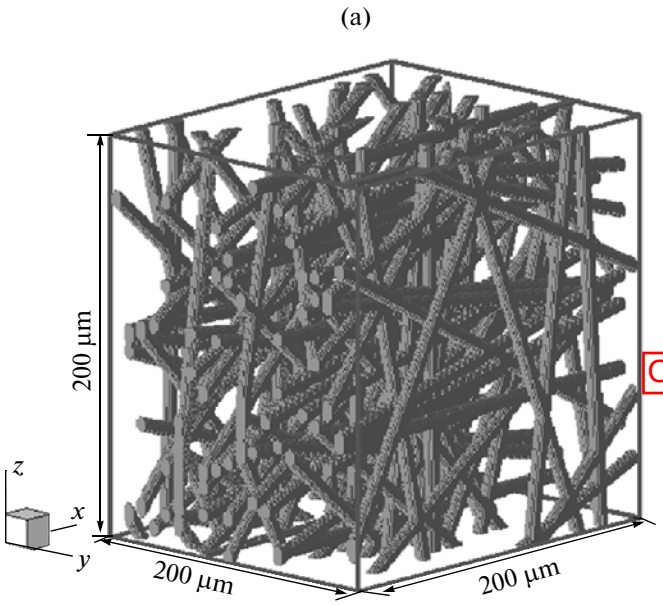

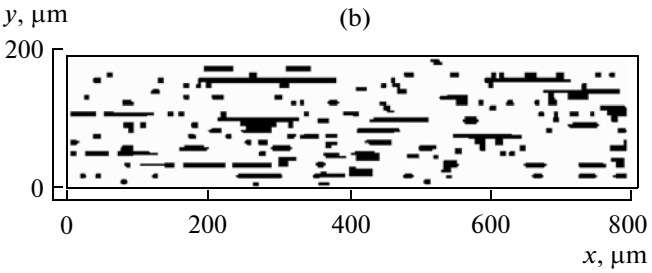

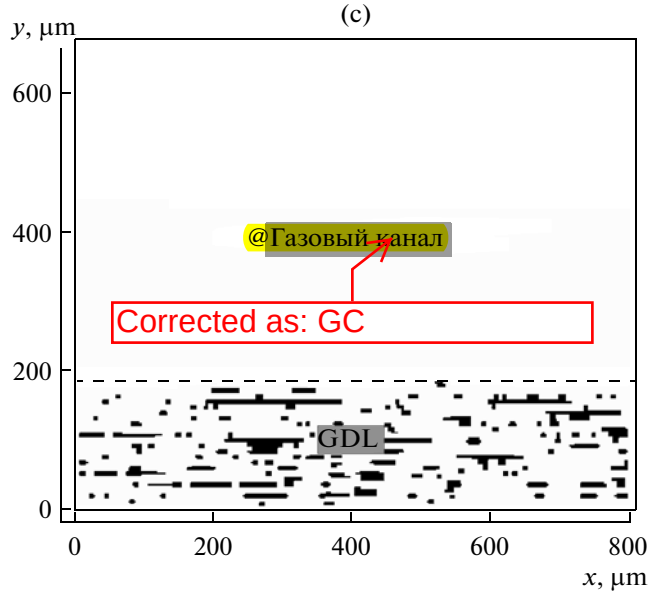

Fig. 2. 3D reconstructed structure of a carbon paper GDL ((a)), a through-plane cross-section slice of the GDL (b) and 2D computation domain ~~contains~~ GC and GDL ((c)).

Corrected as: including

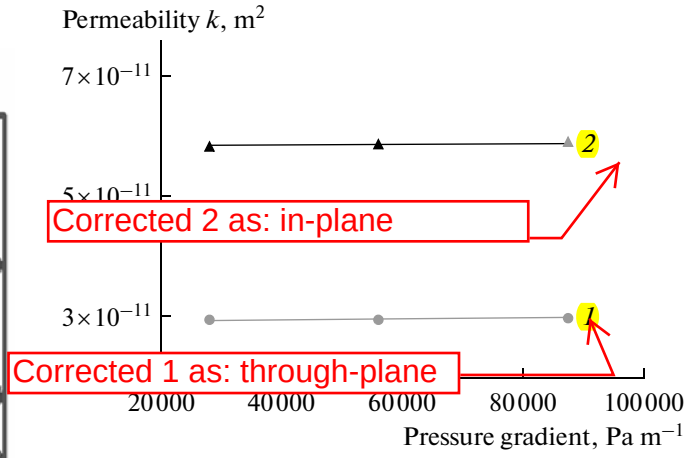

Fig. 3. Numerically predicted permeability of the reconstructed GDL.

In this study, the scale parameters are chosen as $l_0 = 1.0 \times 10^{-6}$ m, $t_0 = 1.33 \times 10^{-8}$ s and $\rho_0 = 1.0$ kg m^{-3}.

3.1. Permeability of the Porous GDL

The permeability is one of the most important macroscopic effective transport properties of the porous GDL, which is inhomogeneous due to the fiber orientation. Usually, the in-plane permeability is higher than the through-plane permeability [5]. To evaluate the permeability of the 2D porous GDL generated in Section 2.2, air flow simulation is performed for the in-plane direction (x direction) and through-plane direction (y direction) using flow LB model introduced in Section 2.1.1, respectively. For in-plane flow, pressure boundaries are specified at the inlet and outlet, respectively (left boundary and right boundary in Fig. 2b), and solid boundaries are specified on the rest surfaces (top and bottom boundaries in Fig. 2b). For the through-plane flow, pressure boundaries are specified on the inlet and outlet, respectively (bottom and top boundaries in Fig. 2b), keeping the rest surfaces as solid boundaries (left and right boundaries in Fig. 2b). The solid obstacles in the domain are impermeable objects with no slip boundary condition on their surfaces. To reduce the influence of the solid obstacles on the inlet and outlet boundaries, fifty more lattices are added on the inlet/outlet boundary as buffer zones. The permeability of the porous GDL can be calculated according to the Darcy' law

$$K = -\frac{\mu \langle u \rangle}{\nabla \langle p \rangle}, \qquad (21)$$

where $\langle u \rangle$ and $\langle p \rangle$ are the superficial velocity and average pressure in the porous GDL respectively.

Figure 3 shows the permeability of the present 2D porous GDL under different pressure gradients. It is clearly shown that the GDL has higher in-plane permeability than through-plane permeability. This is because

more fibers are oriented to the x direction (shown in Fig. 2b). The in-plane and through-plane permeability of Tory 090 with porosity 0.80 measured by Gostick et al. [31] are 2×10^{-11} m^2 and 8.99×10^{-12} m^2, respectively. The simulated results in this study are 5.8×10^{-11} m^2 for the in-plane permeability and2.96×10^{-11} m^2 for the through-plane, which are somewhat greater than the experimental results, partially due to the relatively large porosity (0.87) of the present porous GDL.

3.2. Effective Diffusivity of the Porous GDL

The effective diffusivity is another important macroscopic effective transport property of the porous GDL [5]. Unfortunately, there have been few researches to measure the anisotropic effective diffusivity of the porous GDL [32]. In this study, gas diffusion simulation is performed to evaluate the effective diffusivity of the present 2D porous GDL using mass transport LB model introduced in Section 2.1.2. Concentration fractions are specified on the inlet and outlet, keeping the rest two surfaces as no-flux boundaries. The solid obstacles in the domain are impermeable objects with no flux boundary conditions on their surfaces. Similar to the simulation in Section 3.1, fifty more lattices are added on the inlet/outlet boundary as buffer zones. The effective diffusivity of the porous GDL can be calculated by

$$D_{\mathrm{eff},x} = \frac{D\left(\int_0^H \frac{\partial X}{\partial x} dy\right)/H}{(X_{\mathrm{in}} - X_{\mathrm{out}})/L}, \quad D_{\mathrm{eff},y} = \frac{D\left(\int_0^L \frac{\partial X}{\partial y} dx\right)/L}{(X_{\mathrm{in}} - X_{\mathrm{out}})/H} \quad (22)$$

for in-plane direction and through-plane direction, respectively. D is the binary diffusivity, H and L are the height and length of the present porous GDL, respectively. X_{in} is the inlet concentration fraction and X_{out} is the outlet concentration fraction.

Nam and Kaviany [5] proposed the following correlation to calculate the effective diffusivity of the GDL

$$D_{\mathrm{eff}} = D\varepsilon\left(\frac{\varepsilon - \varepsilon_{\mathrm{p}}}{1 - \varepsilon}\right)^{\alpha}, \quad (23)$$

where $\alpha = 0.521$ for the in-plane direction, $\alpha = 0.785$ for the through-plane direction, and $\varepsilon_{\mathrm{p}} = 0.11$. D_{eff}/D calculated by Eq. (23) for porosity 0.87 is 0.758 and 0.707 for the in-plane direction and through-plane direction, respectively. The simulated D_{eff}/D for the in-plane direction and through-plane direction are 0.771 and 0.713, respectively, which are in good agreement with the values calculated by Eq. (23).

3.3. Evaluation and Calibration of g and w in the Multiphase LB Model

Before ~~explore~~ liquid water behaviors, it is necessary to calibrate g controlling the fluid-fluid interac-

Corrected as: exploring

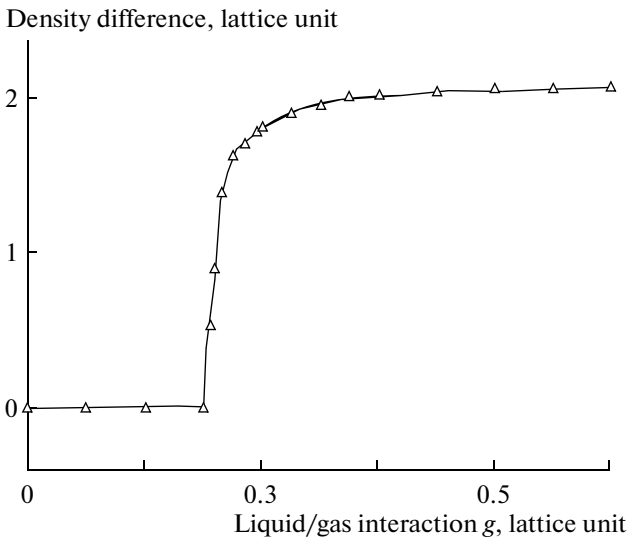

Fig. 4. Difference between the maximum and minimum density of gas as the function of fluid-fluid interaction strength g.

tion and w controlling fluid-solid interaction in SC model. In this regard, two numerical experiments are conducted: bubble test to evaluate g and static droplet contact angle test to determine w.

3.3.1. Bubble test. The bubble test consists of a circular bubble with radius of 20 lattices initially located at the center of a 100×100 lattices system. Based on the work by Huang et al [33], in the bubble initial densities are set as $\rho_1 = 2$ and $\rho_2 = 1 \times 10^{-5}$, and outside the bubble initial densities are set as $\rho_1 = 1 \times 10^{-5}$ and $\rho_2 = 2$, where ρ_1 is the density of gas and ρ_2 is the density of liquid. Periodic boundary conditions are applied on the four boundaries.

Figure 4 shows the difference between the maximum and minimum density of the gas as a function of g. In the SC model, different phases separate with each other only if the absolute value of g exceeds a critical value $2/(9\rho_0)$, where $\rho_0 = \rho_1 + \rho_2$ [33]. It can be seen that in Fig. 4 that the critical value is about 0.22, which is in good agreement with the theoretical value 0.222. When $g < 0.22$, the density difference is zero indicating different phases mix with each other. When $g > 0.22$, the density difference becomes increasing larger, implying different phases start to separate and the bubble becomes increasingly pure. Overlarge g leads to density difference greater than 2.0 as shown in Fig. 4. Thus, g is set as 0.5 in the following simulation.

The pressure difference across the liquid/gas interface is related to the radius R of the bubble by Laplace's Law

$$p_1 - p_0 = \sigma/R, \quad (24)$$

where p_i and p_0 are the pressures inside and outside the bubble, respectively. σ is the surface tension force. Figure 5 shows the pressure difference Δp as a function of

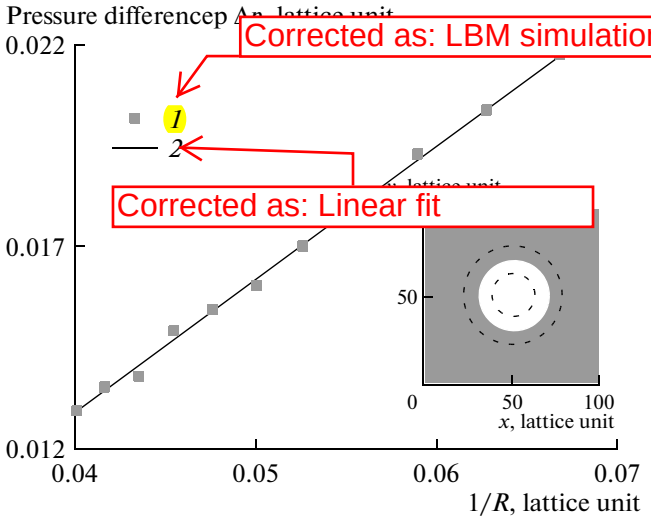

Fig. 5. Pressure difference inside and outside the droplet as a function of the reciprocal of droplet radius $1/R$.

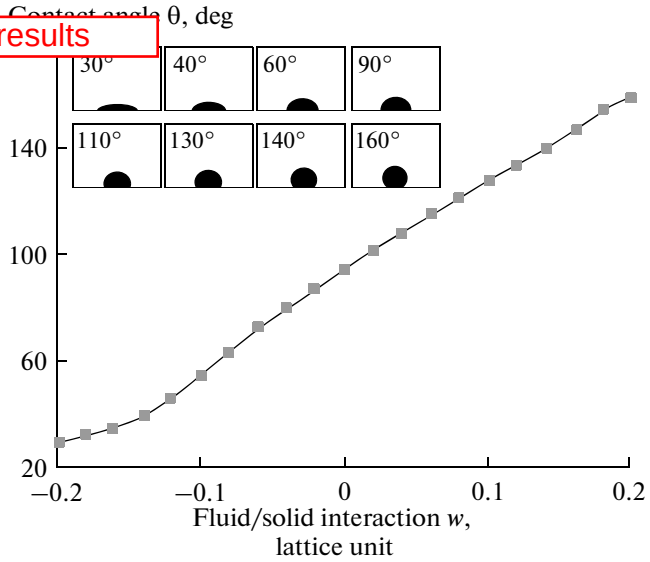

Fig. 6. Contact angles of droplets on the solid surface as a function of fluid-solid interaction w.

$1/R$, where the inserted image shows a bubble with radius 20 (lattice unit) obtained from the simulations, p_i and p_0 are calculated 8 lattices away from the bubble surface, shown by the dashed circles in the inserted image. It can be seen that the pressure difference is proportional to $1/R$, showing a good agreement with Laplace's Law.

3.3.2. Static contact angle test. Contact angle is usually considered as a measure of the solid surface wettability. A surface is wetting or hydrophilic if the contact angle $\theta < 90°$, and liquid tends to spread as film on the solid surface. On the contrary, the surface is non-wetting or hydrophobic if $\theta > 90°$, and liquid tends to form a droplet on the solid surface. A set of initially semicircular static droplets on a horizontal solid surface are simulated to predict different contact angles, with u1 changing from −0.2 to 0.2. Initial densities are set as $\rho_1 = 1 \times 10^{-5}$ and $\rho_2 = 2$ inside the droplet, and $\rho_1 = 2$ and $\rho_2 = 1 \times 10^{-5}$ outside the droplet. Periodic boundary conditions are applied on the left and right boundaries. No slip boundary conditions are used on the bottom and top boundaries. The droplet radius is calculated by the method proposed in [34].

Figure 6 presents the relationship between w and the predicted contact angles, where th corrected as: w shows droplets with different contact angles. Previous literature reported that the contact angle is a linear function of w [33]. The simulation results show this characteristic in the range of w from −0.1 to 0.2. In the following simulation corrected as: w e of the GDL can be obtained by choosing the corresponding w according to Fig. 6.

3.4. Liquid Water Behaviors

In the cathode of a PEMFC, liquid water generated in the CL penetrates through the GDL and finally enters the GC. In the GDL, surface tension force plays a dominant role on liquid water transport and other forces including viscous force, inertial force and gravity force can be negligible [23]. Generally, the relationship between surface tension force and other forces are described by three pertinent non-dimensional numbers including capillary number (Ca, the ratio of viscous force to surface tension force, $\mathrm{Ca} = \mu u/\sigma$), Weber number (We, the ratio of inertial force to surface tension force, $\mathrm{We} = \rho u^2 d/\sigma$) and Bond number (Bo, the ratio of gravity force to surface tension force, $\mathrm{Bo} = (\Delta\rho) d^2 g/\sigma$), where μ is water dynamic viscosity, u liquid water velocity, σ surface tension between water and air, d the characteristic length, $\Delta\rho$ the density difference of liquid water and air and g the gravity acceleration. In the GDL of an operating PEMFC, Ca is of the order 10^{-6}–10^{-8}, Bo is about 10^{-9} and We is of the order 10^{-10} [23], indicating the dominant effects of surface tension force on the liquid water behaviors in the GDL compared to other forces.

On the other hand, in the GC liquid water emerging from the GDL subjected to air flow from the upstream suffers pressure force, shear force, surface n force, gravity, lift force and inertial force. The tion and movement of the liquid water have been widely investigated [35–41]. In a micro GC, the surface tension force also plays an important role on liquid water behaviors. In particular, it overwhelms other forces during the liquid water growth stage [37]. In the present study, only the growth stage of the liquid water in the GC is studied while not concerning the following elongation and detachment stages (For more detail

of the water transport process one can refer to [37]). Therefore, other forces imposed on liquid water also can be neglected compared to the surface tension force in the growth stage of liquid water in the GC.

The above discussions that surface tension force is dominant during liquid water transport within the GDL and the liquid water growth stage in the GC lead to simulations adopting SC model more efficient. In the SC model, numerical simulation process may be instable if density difference and viscosity difference between liquid and gas are too large [22]. As mentioned above, effects of viscous force, gravity and inertial force can be neglected. This implies that density difference and viscosity difference between liquid water and air closely relating to these forces can be ignored. Therefore, density and viscosity of liquid water and air are treated to be equal to each other in GDL as well as in GC in the following simulations using the SC model. Such treatment is also adopted in previous researches using SC model to investigate liquid water behaviors in the GDL [20, 23].

3.4.1. Liquid water behaviors in GDL and GC without land. First the process of liquid water transport in GDL and GC without land is investigated. Initially, air with density as 2.0 occupies the whole computational domain (shown in Fig. 2c). Liquid water density with density 2.0 enters the computational domain from the inlet on the bottom surface. The inlet velocity of liquid water is $8 \times 10^{-7}\ \delta x/\delta t$ in lattice unit and the corresponding Ca is 4×10^{-7} based on the surface tension evaluated in Section 3.1. Air flow is not considered in the GC in the present study and thus air velocity in the GC and GDL is initially specified as zero. The relaxation time r related to dynamic viscosity is set as 1 for both fluid corrected as: τ cosities as 1/6 in lattice units. The GDL and GC are hydrophobic with contact angle as 120°. Periodic boundary conditions are applied on the left and right boundaries and no-slip boundary conditions are adopted for the bottom and top boundaries. In addition, no-slip boundary conditions are used for all the soli Corrected as: gray fibers in the GDL.

Figure 7 shows the liquid water transport processes within the GDL from the water inlet to the GDL-GC interface. In Fig. 7, blue is liquid water, light yellow denotes air and black represents carbon fibers. Liquid water always preferentially chooses the largest pores to invade on its advancing path as shown in Fig. 7, since larger hydrophobic pores create smaller resistance force [6]. As a result, when liquid water reaches the GDL-GC interface, a flexuous pat Corrected as: white water which always occupies largest pores is formed inside the GDL (shown in Fig. 7c), which agrees with the simulations results in [23, 24].

Figure 8 displays the liquid water behaviors near the GDL-GC interface and in the GC. At the interface, two pores (shown in the red circles in Fig. 8a) are possibly available for liquid water to ingress into the GC. Howev Delete is a little larger than that in the right circle *2*, implying smaller resistance in the left circle. Thus, liquid water enters GC through the left pore and forms a droplet under the dominant surface tension force. At the same time, liquid water in the right circle start to recede due to the preferential pathway formed in the left circle, as shown in Fig. 8b. Subsequently, the droplet gradually grows and liquid water in the right circle continuously withdraws, as shown by the arrows in Fig. 8c. This phenomenon is consistent with the experimental observation suggesting a dynamic interconnection of water pathways in the GDL [8].

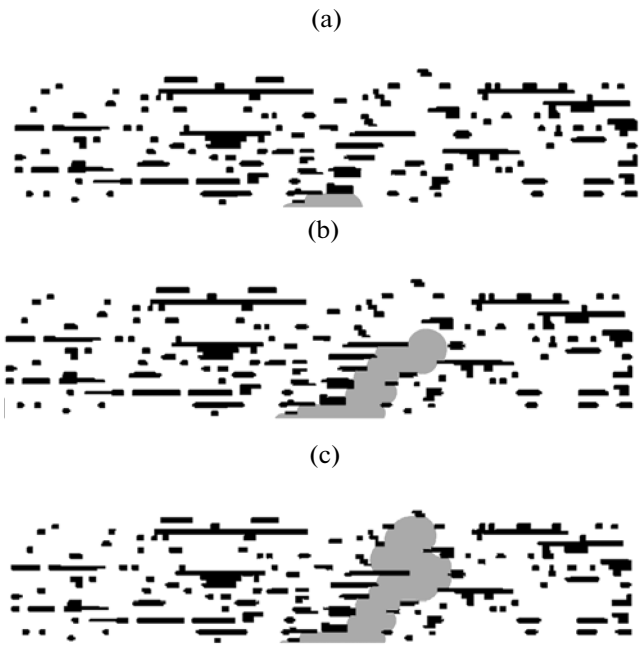

Fig. 7. Liquid water transport process from inlet to GDL-GC interface at different time step: (a) $t = 50000$ time step, (b) $t = 250000$ time step, (c) $t = 280000$ time step.

It be noted that in literature [8] the water injection rate is relatively high, and thus the corresponding Ca is larger than the typical Ca in GDL of PEMFC. Larger Ca may results in liquid water transport mechanism changing from capillary fingering to stable front invasion [22]. Thus, it is critical to match Ca in experiments or simulations with that in practical operating PEMFC. Although Ca in [8] is relatively higher compared to that in PEMFC, numerical results with reasonable Ca in this study confirms the experi-] that pathway of liquid water within the GDL is dynamic interconnected.

3.4.2. Liquid water behaviors in GDL and GC with a land. When liquid water permeates through GDL and reaches GDL-GC interface, it also may touch the bottom surface of a land. Obviously, the land wettability will greatly affect liquid water transport processes near the land. Thus, effects of land wettability are investi-

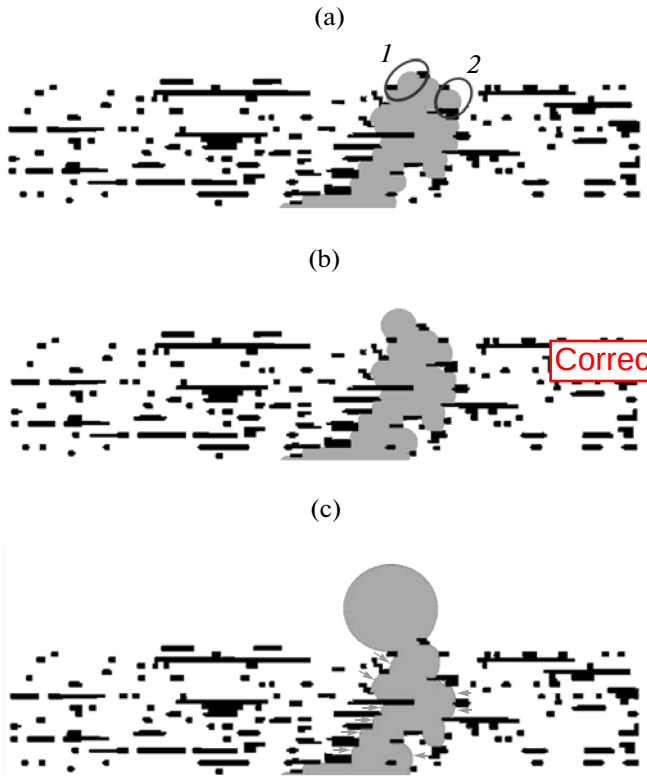

Fig. 8. Liquid water transport process near the GDL-GC interface and in the GC at different time steps: (a) t = 310000 time step, (b) t = 330000 time step, (c) t = 370000 time step.

gated by adding a rectangular land in the following simulation.

A land is positioned from $x = 350$ to $x = 650$ in the x direction in the GC, as shown in Fig. 9a. Such placement covers the local GDL-GC interface where a droplet forms in the without land case in Section 3.3.1. For the hydrophilic land case, the contact angles of channel walls, including the bottom surface and two side surfaces of the land, as well as the top wall of the channel, are set as 60°, which are set as 120° for hydrophobic land case. The GDL is hydrophobic. All the other boundary and initial conditions are the same as that in the without land case in Section 3.3.1. It is worth mentioned that the pore sizes near the GDL/land interface are smaller than that within the GDL in this study, which is practical due to compression of the components of PEMFC under significant pressure [42].

Corrected as: mentioning

Figures 9 and 10 show the time evolution of liquid water distribution in GDL and GC to illuminate the effects of channel wall wettability on liquid water distributions. In Fig. 9 the channel wall surfaces are hydrophilic, whereas in Fig. 10 the channel wall surfaces are hydrophobic. The distinguished difference between Figs. 9 and 10 is that liquid water tends to spread as film on the hydrophilic land surfaces, whereas a droplet is formed in the GC with hydrophobic land surfaces. This is consistent with the experimental results in [14]. Besides, liquid water still preferentially chooses the largest pores to invade on its advancing path in the hydrophobic GDL, as shown in Figs. 9 and 10. When liquid water arrives near the GDL/land interface, compared to the without land case in Fig. 8, in Figs. 9c and 10b liquid water chooses the right pore in red circle *2* to invade. This is because the size of the two pores in circles *1* and *2* (Liquid water chooses to enter the GC in the without land case) reserves, as shown in Fig. 9c. Thus, at this time ght pore to invade and arrives at the GDL/land interface.

Corrected as: delete

Interesting phenomenon can be observed when liquid water transports at the GDL/land interface, as shown in circle *3* Figs. 9d and 10c. The pathway for liquid water at the interface is completely hydrophobic for the hydrophobic land case (hydrophobic land bottom surface and hydrophobic GDL top surface). However, it is partially hydrophobic for the hydrophilic land case (hydrophilic land bottom surface and hydrophobic GDL top surface). Thus, it is expected that capillary pressure required for liquid water advancing at the GDL/hydrophobic land interface is higher than that at the GDL/hydrophilic land interface. Obviously, higher capillary pressure at the GDL/land i results in more liquid water accumulated wit d pathway of liquid water inside the GDL [8]. Thus, more liquid water will accumulates within the GDL under the hydrophobic land than that under the hydrophilic land, which is consistent with the experimental results in [14]. The phenomenon is more obvious in Fig. 11. Figure 11 shows the time evolution of liquid water saturation within the GDL. The water saturation S is defined as the radio of pore volume filled by liquid water to the total dry pore volume. In Fig. 11, the liquid water saturation within the GDL under the hydrophobic land is greater than that under the hydrophilic land, which is expected based on the above discussion. Since liquid water distribution in the GDL greatly affects reactant transport and thus the cell performance, the impact of channel wall wettability on liquid water saturation in GDL should be taken into account in studies regarding mass transport and fluid flow in PEMFC.

Corrected as: accumulate

3.5. Wetter Transport in GDL with Different Wettability

Delete

In this section, liquid water distributions in GDL are investigated for six cases with different wettability. GDL is completely hydrophobic GDL in Case 1 and is completely hydrophilic in Case 2. Half region of the GDL is hydrophobic in Cases 3-6 with different distribution of the hydrophobic region, as shown in Figs. 12c–12f. In Figs. 12c–12f, regions marked 1 denote hydrophilic regions and that marked 2 denote hydrophobic regions, with hydrophobic and hydro-

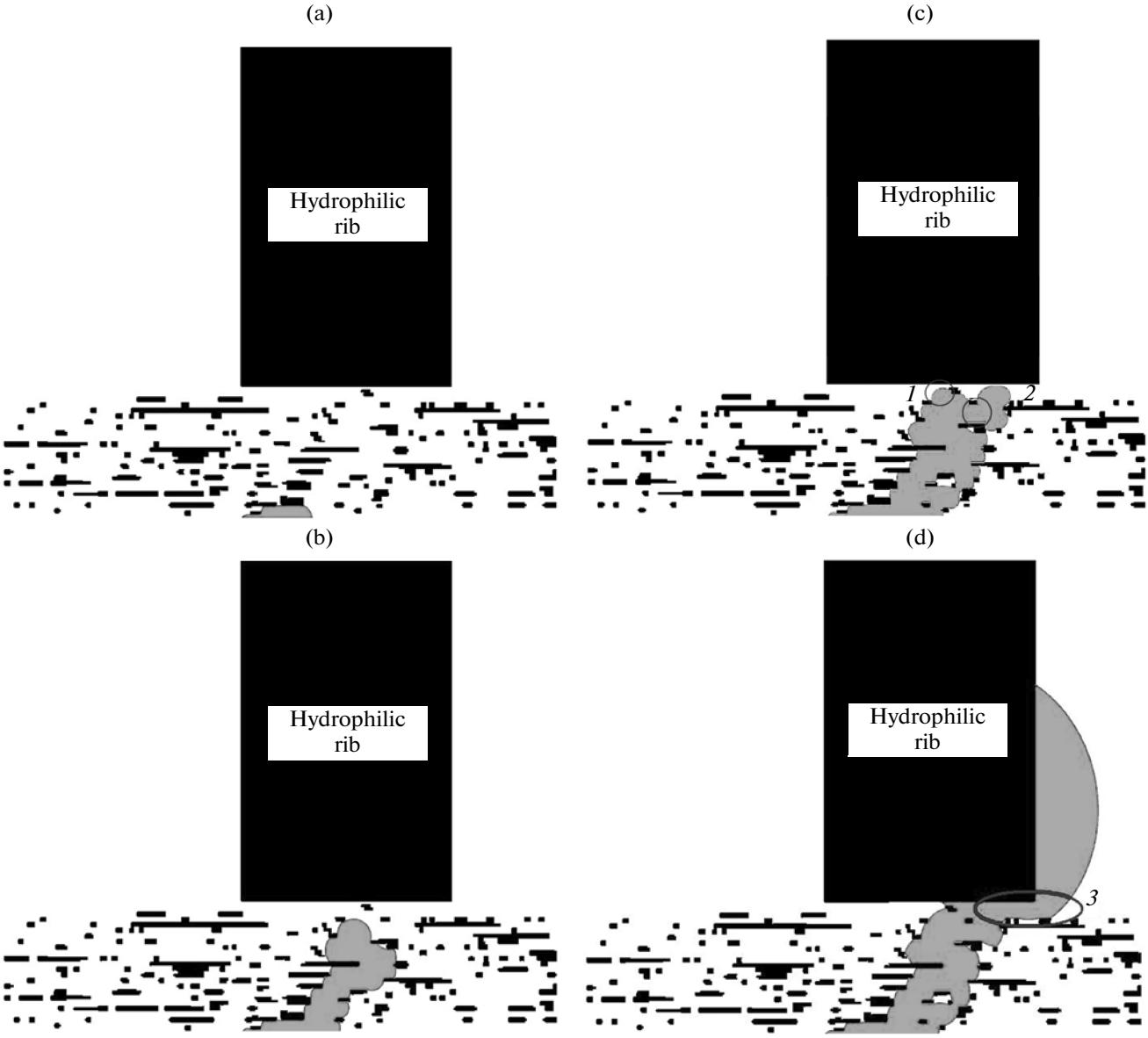

Fig. 9. Liquid water transport process in the GDL and GC with a hydrophilic land: (a) $t = 50000$ time step, (b) $t = 150000$ time step, (c) $t = 200000$ time step, (d) $t = 300000$ time step.

philic regions separated by the solid lines. Practically, the distribution of hydrophilic and hydrophobic regions in GDL due to PTFE treatment is very complex [43], and the four square patch-wise distribution patterns shown in Figs. 12c–12f may be regarded as simplified models.

Followed the method proposed in [23], liquid water is initially randomly distributed throughout the computational domain (shown in Fig. 2b) with specified averaged water saturation (in this study 0.2 for all the cases). Body forces are added to both liquid water and gas along y direction to simulate counter-current flow [23]. Liquid water and gas will redistribute during the simulation until the steady state is achieved. No-slip boundary conditions are used for the left and right boundaries. Periodic boundary conditions are applied on the bottom and top boundaries.

Figure 12 displays liquid water distributions for the six cases. Clearly, different wettability of the GDL creates distinct liquid water distribution patterns. Generally, liquid water in hydrophobic regions exhibits as isolated droplets adjacent to the carbon fibers, similar to the experimental results in [5]. In the hydrophilic regions, however, liquid water tends to spread on the carbon fiber surfaces as thin films. Besides, the distribution of water film is more agglomerate compared with that in hydrophobic regions. For Cases 3–6 with mixed wettabilities, liquid water distribution patterns

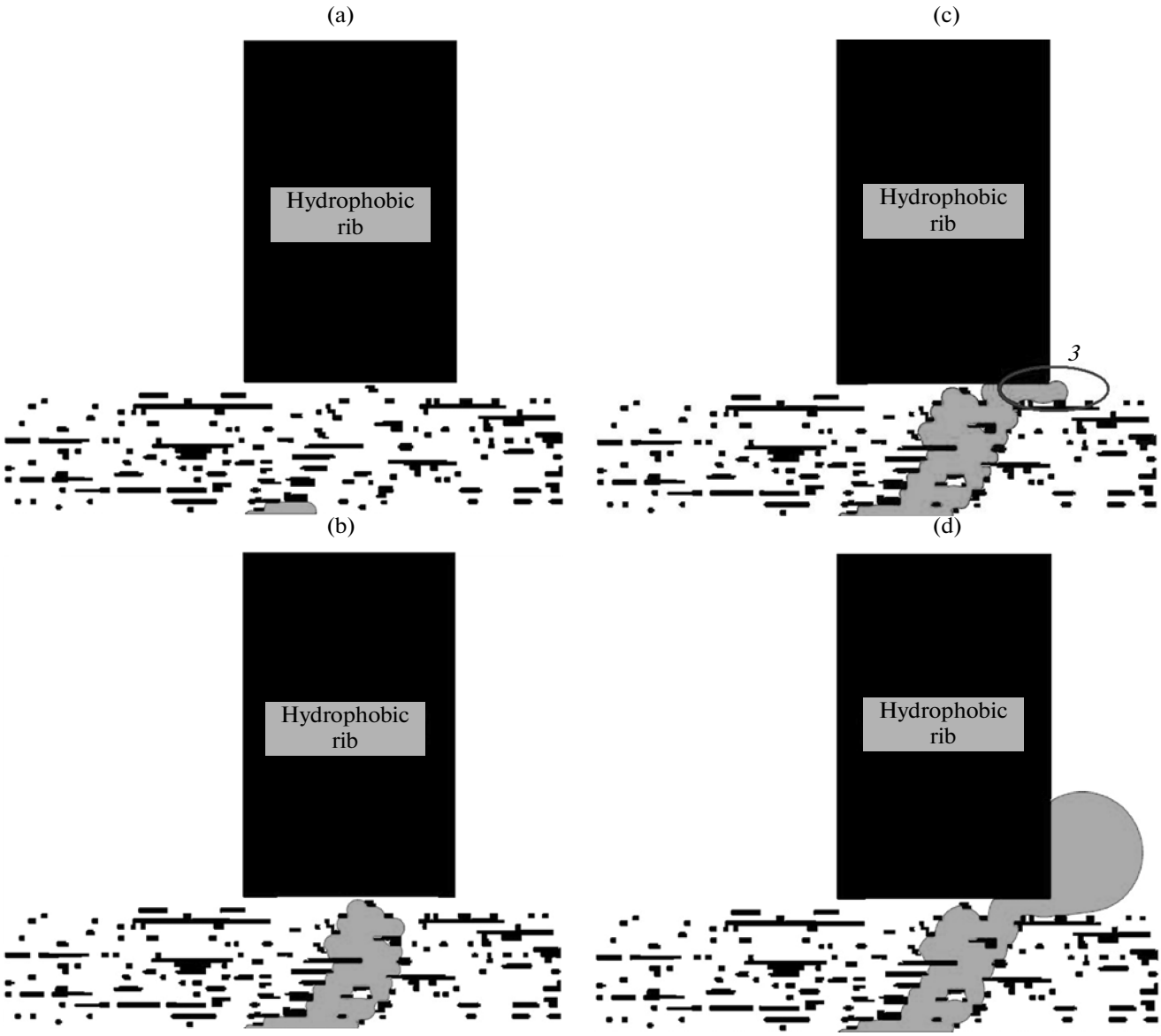

Fig. 10. Liquid water transport process in the GDL and GC with a hydrophobic land: (a) $t = 100000$ time step, (b) $t = 300000$ time step, (c) $t = 360000$ time step, (d) $t = 460000$ time step.

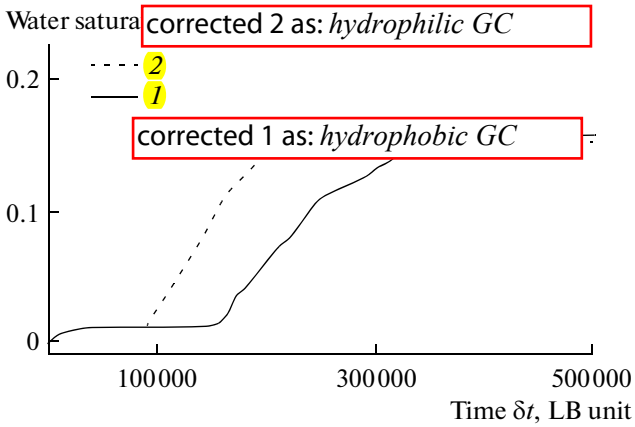

Fig. 11. Time evolutions of liquid water saturation within the GDL under a hydrophobic land and a hydrophilic land respectively.

quite differ from each other although the areas of the hydrophobic regions are the same or in the other word, the PTFE content is the same for the four cases. This implies that an averaged PTFE content itself cannot describe the pore-scale liquid water distribution in the GDL, and the detailed distributions of hydrophilic and hydrophobic regions are further required to reveal the specific characteristics of liquid water distribution.

It is noticeable that for all the simulation results, liquid water is separately distributed as films or droplets (Such distribution of liquid water is called as separated distribution in this study) without forming continuous capillary flow. This separated distribution corresponds to ex situ experimental results of Nam and Kaviany [5] in which liquid water vapor condenses randomly in GDL as small droplets or films and has

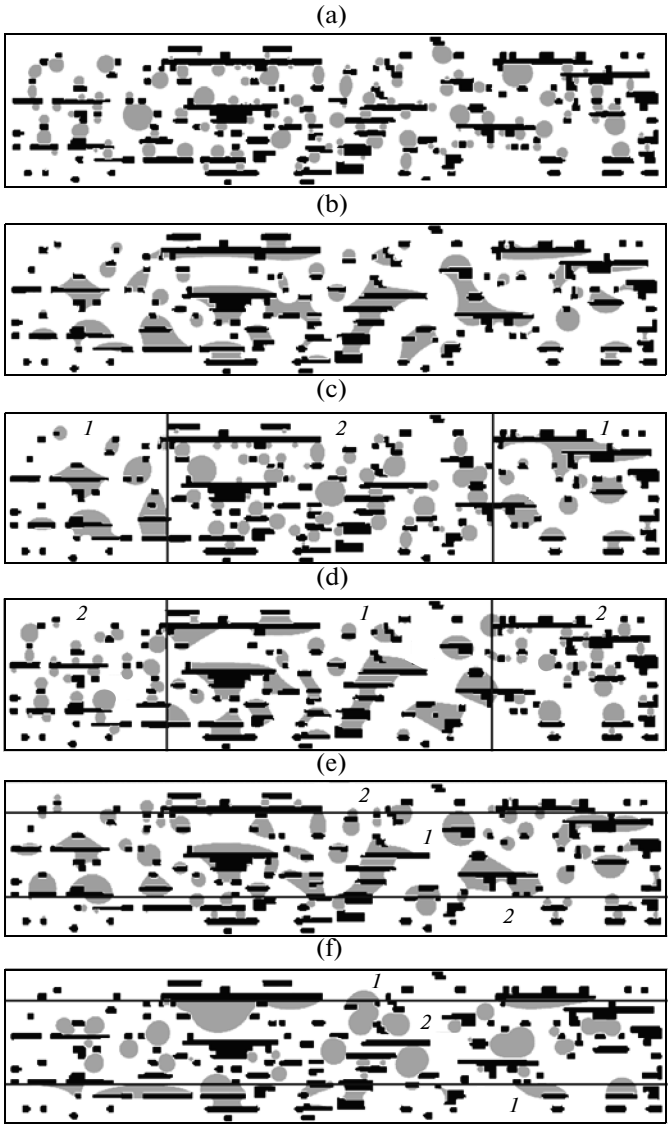

Fig. 12. Liquid water distribution in GDL with different wettability for liquid water saturation of 0.2. (a) Case 1 completely hydrophobic; (b) Case 2 completely hydrophilic; (c) Case 3 (1 denotes hydrophilic region, 2 denotes hydrophobic region); (d) Case 4 (1 denotes hydrophilic region, 2 denotes hydrophobic region); (o) Case 5 (*1* denotes hydrophilic region, *2* denotes hydrophobic region); (f) Case 6 (*1* denotes hydrophilic region, *2* denotes hydrophobic region).

not achieved the saturation level for forming continuous capillary flow. Recently, in situ experiment using neutron image by Turhan et al. [14] also have observed this separated distributions for a short duration after cell start-up in an operating PEMFC.

The effective diffusivity of GDL is an important parameter which reflects reactant diffusion efficiency. The effective diffusivity of GDL reduces if liquid water accumulates in GDL as it restricts the reactant diffusion by reducing the diffusion area and creating tortuous diffusion path. Thus, the effective diffusivities for the six cases with different water distributions are evaluated using the mass transport LB model introduced in Section 2.1.2.

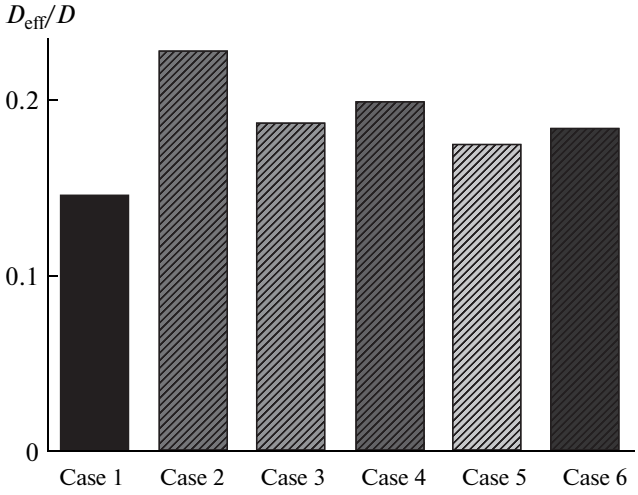

Fig. 13. Effective diffusivities of GDL with different wettability.

Figure 13 presents D_{eff}/D numerically predicted for the six cases. It can be seen that although the water saturation is at the same level, D_{eff} for different cases differs from each other due to different liquid water distribution inside the GDL. Interestingly, D_{eff} for Case 2 with completely hydrophilic GDL is the highest while that for Case 1 with completely hydrophobic GDL is the lowest. This is because tall droplets can more seriously block the void space in the GDL than the water film spreading on the solid surfaces, as shown in Fig. 12. This implies that a hydrophilic GDL is beneficial for reactant transport if liquid water presents as separated distributions. On the contrary, previous study has found out that a hydrophobic GDL is more desirable if liquid water forms continuous capillary flow [10], as liquid water only flows in certain preferential pathways and leaves most of the GDL pores available for reactant transport in a hydrophobic GDL. The discrepancy indicates that whether PTFE treatment is beneficial for cell performance depends on the detail distributions of liquid water within the GDL and PTFE treatment doesn't directly means superior cell performance. In fact, results of experiments regarding effects of PTFE treatment on cell performance also vary from each other sometimes [44–46]. Shimpalee et al. [44] found that the cell performance obtained with hydrophilic GDL is significantly lower than that with hydrophobic GDL because of severe flooding in hydrophilic GDL. On the contrary, Tuber et al. [45] reported that PMEFC with hydrophilic GDL performed better. Park et al. [46] found that the higher the PTFE content in GDL, the lower the cell performance.

Actually, water transport in porous GDL is indeed a significantly complex process due to various affected factors including GDL thickness, GDL porosity, GDL wettability and pore sizes. Therefore, it is not surprising that different liquid water distribution patterns inside the GDL have been observed, and it is understandable that PEMFC with hydrophobic GDL doesn't always perform better under different operating conditions [44–46].

4. CONCLUSIONS

In this study, LBM is used to investigate liquid water transport behaviors in GDL. A porous GDL obtained from reconstruction processes is used in the simulation. Effects of GC and GDL wettability on liquid water distribution are explored. The main conclusions are derived as follows:

(1) Within the hydrophobic GDL, liquid water transport mechanism is capillary fingering and the pathway of liquid water is dynamic interconnected.

(2) The GC wall wettability significantly affects the liquid water content within the GDL and a hydrophobic GC leads to more liquid water accumulated in the GDL compared to a hydrophilic GC.

(3) Liquid water presents different distribution patterns in GDL with different wettability. PTFE content itself cannot determine liquid water distribution within the GDL and the detailed distributions of hydrophobic and hydrophilic regions also play an important role;

(4) If liquid water presents as separated distribution in the GDL in which liquid water shows as separated droplets or films, effective diffusivity of reactants in a hydrophilic GDL is higher than that in a hydrophobic GDL. Thus, a hydrophobic GDL doesn't always result in better performance of PEMFC.

ACKNOWLEDGMENTS

This work is supported by the Key Project of the National Natural Science Foundation of China (50636050).

corrected as: *51136004*

NOMENCLATURE

c_s—speed of sound in LBM

C_O—oxygen concentration, mol m^{-3}

C_Q—lattice dependent coefficient in Eq. (12)

D diffusivity, m^2 s^{-1}

e_i—discrete velocity in LBM

f_i—particle distribution function in the ith direction

f_i^{eq}—equilibrium particle distribution function

F—Faraday's constant, C mol^{-1}

$F_{a,k}$—fluid-solid interaction force in SC model

$F_{c,k}$—fluid-fluid surface tension acting on kth component in SC model

F_k—forces acting on kth component

g—parameter control strength between different component in SC model

$G_{k\bar{k}}$—Green funciton in SC model

J_i—specially chosen constant in Eq. (8)

K_i—specially chosen constant in Eq. (8)

l_0—length scale

p—Pressure, Pa

$\langle p \rangle$—average pressure, Pa

R—universal gas constant, J mol^{-1} K^{-1}

s—an indicator function in SC model for solid phase

S—source term in mass transport LB model

t—time

t_0—time scale

t—time step

T—temperature of the operation condition, K

$\mathbf{u}$—local velocity, m s^{-1}

$\mathbf{u}'$—common velocity for all of the phases in SC model, m s^{-1}

$\langle u \rangle$—superficial velocity, m s^{-1}

w—parameter controls strength between fluid and wall in SC model

w_i—weight factor in equilibrium particle distribution function

W—Green funciton SC model

x—position

Δx—mesh width

X_k—mole fraction of kth species

Greek Symbol

ε—porosity

ε_p—parameter in Eq. (23)

σ—surface tension

ν—Kinetic viscosity

ρ—Density

τ—relaxation time

τ_v—relaxation time related to viscosity

τ_D—relaxation time related to diffusivity

ψ_k—effective density in SC model

Subscripts and Superscripts

L—lattice unit

p—physical unit

REFERENCES

1. Li, H., Tang, Y., Wang, Z., Shi, Z., Wu, S., Song, D., Zhang, J., Fatih, K., Zhang, J., Wang, H., Liu, Z., Abouatallah, R., and Mazza, A., A Review of Water Flooding Issues in the Proton Exchange Membrane

Fuel Cell, *Journal of Power Sources*, 2008, vol. 178, pp. 103–117.

2. Bazylak, A., Liquid Water Visualization in PEM Fuel Cells: A Review, *International Journal of Hydrogen Energy*, 2009, vol. 34, pp. 3845–3857.
3. Anderson, R., Zhang, L., Ding, Y., Blanco, M., Bi, X., and Wilkinson, D.P., A Critical Review of Two-Phase Flow in Gas Flow Channels of Proton Exchange Membrane Fuel Cells, *Journal of Power Sources*, 2010, vol. 195, pp. 4531–4553.
4. Lenormand, R., Numerical Models and Experiments on Immiscible Displacements in Porous Media, *Journal of Fluid Mechanics*, 1988, vol. 189, pp. 165–118.
5. Nam, J.H. and Kaviany, M., Effective Diffusivity and Water-Saturation Distribution in Single- and Two-Layer PEMFC Diffusion Medium, *International Journal of Heat and Mass Transfer*, 2003, vol. 46, pp. 4595–4611.
6. Litster, S., Sinton, D., and Djilali, N., Ex Situ Visualization of Liquid Water Transport in PEM Fuel Cell Gas Diffusion Layers, *Journal of Power Sources*, 2006, vol. 154, pp. 95–105.
7. Bazylak, A., Sinton, D., Liu, Z.S., and Djilali, N., Effect of Compression on Liquid Water Transport and Microstructure of PEMFC Gas Diffusion Layers, *Journal of Power Sources*, 2007, vol. 163, pp. 784–792.
8. Bazylak, A., Sinton, D., and Djilali, N., Dynamic Water Transport and Droplet Emergence in PEMFC Gas Diffusion Layers, *Journal of Power Sources*, 2008, vol. 176, pp. 240–246.
9. Gao, B., Steenhuis, T.S., Zevi, Y., Parlange, J.Y., Carter, R.N., and Trabold, T.A., Visualization of Unstable Water Flow in a Fuel Cell Gas Diffusion Layer, *Journal of Power Sources*, 2009, vol. 190, pp. 493–498.
10. Pasaogullari, U. and Wang, C.Y., Liquid Water Transport in Gas Diffusion Layer of Polymer Electrolyte Fuel Ceils, *Journal of the Electrochemical Society*, 2004, vol. 151, pp. A399–A406.
11. Manke, I., Hartnig, C., Grünerbel, M., Lehnert, W., Kardjilov, N., Haibel, A., Hilger, A., Banhart, J., and Riesemeier, H., Investigation of Water Evolution and Transport in Fuel Cells with High Resolution Synchrotron X-Ray Radiography, *Applied Physics Letters*, 2007, vol. 2007, p. 174105.
12. Adam, Z.W. and John, N., Coupled Thermal and Water Management in Polymer Electrolyte Fuel Cells, *Journal of the Electrochemical Society*, 2006, vol. 153, pp. A2205–A2214.
13. Soowhan, K. and Mench, M.M., Investigation of Temperature-Driven Water Transport in Polymer Electrolyte Fuel Cell: Phase-Change-Induced Flow, *Journal of The Electrochemical Society*, 2009, vol. 156, pp. B353–B362.
14. Turhan, A., Kim, S., Hatzell, M., and Mench, M.M., Impact of Channel Wall Hydrophobicity on Through-Plane Water Distribution and Flooding Behavior in a Polymer Electrolyte Fuel Cell, *Eleclrochimica Acta*, 2009, vol. 55, pp. 2734–2745.
15. Voltkovich, Y.M., Sosenkin, V.E., Nikol'skaya, N.F., and Kulova, T.L., Porous Structure and Hydrophilic-Hydrophobic Properties of Gas Diffusion Layers of the Electrodes in Proton-Exchange Membrane Fuel Cells, *Russian Journal of Electrochemistry*, 2008, vol. 44, pp. 278–285.
16. Volfkovich, Y.M., Sosenkin, V.E., and Bagotsky, V.S., Structural and Wetting Properties of Fuel Cell Components, *Journal of Power Sources*, 2010, vol. 195, pp. 5429–5441.
17. Chen, S.Y. and Doolen, G.D., Lattice Boltzmann Methode for Fluid Flows, *Annual Review of Fluid Mechanics,* 1998, vol. 30, pp. 329–364.
18. Park, J., Matsubara, M., and Li, X., Application of Lattice Boltzmann Method to a Micro-Scale Flow Simulation in the Porous Electrode of a PEM Fuel Cell, *Journal of Power Sources*, 2007, vol. 173, pp. 404–414.
19. Hao, L. and Cheng, P., Lattice Boltzmann Simulations of Anisotropic Permeabilities in Carbon Paper Gas Diffusion Layers, *Journal of Power Sources*, 2009, vol. 186, pp. 104–114.
20. Park, J. and Li, X., Multi-Phase Micro-Scale Flow Simulation in the Electrodes of a PEM Fuel Cell by Lattice Boltzmann Method, *Journal of Power Sources*, 2008, vol. 178, pp. 248–257.
21. Niu, X.D., Munekata, T., Hyodo, S.A., and Suga, K., An Investigation of Water-Gas Transport Processes in the Gas-Diffusion-Layer of a PEM Fuel Cell by a Multiphase Multiple-Relaxation-Time Lattice Boltzmann Model, *Journal of Power Sources*, 2007, vol. 172, pp. 542–552.
22. Puneet K. Sinha, P. Mukherjee P., and Wang, C.Y., Impact of GDL Structure and Wettability on Water Management in Polymer Electrolyte Fuel Cells, *J. Mater. Chem.,* 2007, vol. 17, pp. 3089–3103.
23. Mukherjee, P.P., Wang, C.Y., and Kang, Q., Mesoscopic Modeling of Two-Phase Behavior and Flooding Phenomena in Polymer Electrolyte Fuel Cells, *Electrochimica Acta*, 2009, vol. 54, pp. 6861–6875.
24. Hao, L. and Cheng, P., Lattice Boltzmann Simulations of Water Transport in Gas Diffusion Layer of a Polymer Electrolyte Membrane Fuel Cell, *Journal of Power Sources*, 2010, vol. 195, pp. 3870–3881.
25. Bhatnagar, P.L., Gross, E.P., and Krook, M., A Model for Collision Processes in Gases. I. Small Amplitude Processes in Charged and Neutral One-Component Systems, *Physical Review*, 1954, vol. 94, p. 511.
26. Dawson, S.P., Chen, S., and Doolen, G.D., Lattice Boltzmann Computations for Reaction-Diffusion Equations, *Journal of Chemical Physics*, 1993, vol. 98, pp. 1514–1523.
27. Sullivan, S.P., Sani, F.M., Johns, M.L., and Gladden, L.F., Simulation of Packed Bed Reactors Using Lattice Boltzmann Methods, *Chemical Engineering Science*, 2005, vol. 60, pp. 3405–3418.
28. Shan, X. and Chen, H., Lattice Boltzmann Model for Simulating Flows with Multiple Phases and Components, *Physical Review E*, 1993, vol. 47, pp. 1815–1819.
29. Shan, X. and Doolen, G., Multicomponent Lattice-Boltzmann Model with Interparticle Interaction, *Journal of Statistical Physics*, 1995, vol. 81, pp. 379–393.
30. Martys, N.S. and Chen, H., Simulation of Multicomponent Fluids in Complex Three-Dimensional Geometries by the Lattice Boltzmann Method, *Physical Review E,* 1996, vol. 53, pp. 743–750.

31. Gostick, J.T., Fowler, M.W., Pritzker, M.D., Ioannidis, M.A., and Behra, L.M., In-Plane and Through-Plane Gas Permeability of Carbon Fiber Electrode Backing Layers, *Journal of Power Sources*, 2006, vol. 162, pp. 228–238.
32. Pharoah, J.G., Karan, K., and Sun, W., On Effective Transport Coefficients in PEM Fuel Cell Electrodes; Anisotropy of the Porous Transport Layers, *Journal of Power Sources*, 2006, vol. 161, pp. 214–224.
33. Huang, H., Thorne, D.T., Schaap, M.G., and Sukop, M.C., Proposed Approximation for Contact Angles in Shan-and-Chen-Type Multicomponent Multiphase Lattice Boltzmann Models, *Physical Review E*, 2007, vol. 76, p. 066701.
34. Dullien, F., *Porous Media: Fluid Transport and Pore Structure*, San Diego: Academic Press, 1992.
35. Theodorakakos, A., Ous, T., Gavaises, M., Nouri, J.M., Nikolopoulos, N., and Yanagihara, H., Dynamics of Water Droplets Detached from Porous Surfaces of Relevance to PEM Fuel Cells, *Journal of Colloid and Interface Science*, 2006, vol. 300, pp. 673–687.
36. Zhu, X., Sui, P.C., and Djilali, N., Dynamic Behaviour of Liquid Water Emerging from a GDL Pore into a PEMFC Gas Flow Channel, *Journal of Power Sources*, 2007, vol. 172, pp. 287–295.
37. Zhu, X., Sui, P.C., and Djilali, N., Three-Dimensional Numerical Simulations of Water Droplet Dynamics in a PEMFC Gas Channel, *Journal of Power Sources*, 2008, vol. 181, pp. 101–115.
38. Le, A.D. and Zhou, B., A Generalized Numerical Model for Liquid Water in a Proton Exchange Membrane Fuel Cell with Interdigitated Design, *Journal of Power Sources*, 2009, vol. 193, pp. 665–683.
39. Zhu, X., Liao, Q., Sui, P.C., and Djilali, N., Numerical Investigation of Water Droplet Dynamics in a Low-Temperature Fuel Cell Microchannel: Effect of Channel Geometry, *Journal of Power Sources,* 2010, vol. 195, pp. 801–812.
40. Ding, Y., Bi, H.T., and Wilkinson, D.P., Three-Dimensional Numerical Simulation of Water Droplet Emerging from a Gas Diffusion Layer Surface in Micro-Channels, *Journal of Power Sources*, 2010, vol. 195, pp. 7278–7288.
41. Le, A.D., Zhou, B., Shiu, H.-R., Lee, C.-I., and Chang, W.-C., Numerical Simulation and Experimental Validation of Liquid Water Behaviors in a Proton Exchange Membrane Fuel Cell Cathode with Serpentine Channels, *Journal of Power Sources*, 2010, vol. 195, pp. 7302–7315.
42. Roshandel, R., Farhanieh, B., and Saievar-Iranizad, E., The Effects of Porosity Distribution Variation on PEM Fuel Cell Performance, *Renewable Energy*, 2005, vol. 30, pp. 1557–1572.
43. Gostick, J.T., Fowler, M.W., Ioannidis, M.A., Pritzker, M.D., Volfkovich, Y.M., and Sakars, A., Capillary Pressure and Hydrophilic Porosity in Gas Diffusion Layers for Polymer Electrolyte Fuel Cells, *Journal of Power Sources*, 2006, vol. 156, pp. 375–387.
44. Shimpalee, S., Beuscher, U., and Van Zee, J.W., Analysis of GDL Flooding Effects on PEMFC Performance, *Electrochimica Acta*, 2007, vol. 52, pp. 6748–6754.
45. Tüber, K., Pócza, D., and Hebling, C., Visualization of Water Buildup in the Cathode of a Transparent PEM Fuel Cell, *Journal of Power Sources,* 2003, vol. 124, pp. 403–414.
46. Park, G.G., Sohn, Y.J., Yang, T.H., Yoon, Y.G., Lee, W.Y., and Kim, C.S., Effect of PTFE Contents in Gas Diffusion Media on the Performance of PEMFC, *Journal of Power Sources*, 2004, vol. 131, pp. 182–187.

SPELL: 1. ok